ACADÉMIE
DES SCIENCES
INSTITUT DE FRANCE

Comptes Rendus
Mécanique

Christelle J. Combescure, Nicolas Auffray, Marc L.M. François and Nassim Kesmia

Linking material symmetry and domain of elastic behavior: new numerical insights

Volume 354 (2026), p. 543-560

Online since: 4 June 2026

https://doi.org/10.5802/crmeca.364

The Comptes Rendus. Mécanique *are a member of the Mersenne Center for open scientific publishing*
www.centre-mersenne.org — e-ISSN : 1873-7234

ACADÉMIE DES SCIENCES
INSTITUT DE FRANCE

Comptes Rendus. Mécanique
2026, Vol. 354, p. 543-560
https://doi.org/10.5802/crmeca.364

Research article

Linking material symmetry and domain of elastic behavior: new numerical insights

Christelle J. Combescure [a,*,a,b], **Nicolas Auffray** [c], **Marc L.M. François** [d] **and Nassim Kesmia** [e]

[a] CREC Saint-Cyr, Académie Militaire de Saint-Cyr Coetquidan, F-56380 Guer, France

[b] Univ. Bretagne Sud, UMR CNRS 6027, IRDL, F-56100, Lorient, France

[c] Sorbonne Université, CNRS, Institut Jean Le Rond d'Alembert, F-75005 Paris, France

[d] Nantes Université, École Centrale Nantes, CNRS, GeM, UMR 6183, F-44000 Nantes, France

[e] DMAS, ONERA, Université Paris Saclay, F-92322 Châtillon, France

E-mails: c.combescure@st-cyr.terre-net.defense.gouv.fr, nicolas.auffray@sorbonne-universite.fr, marc.francois@univ-nantes.fr, nassim.kesmia@onera.fr

Abstract. In the context of the growing industrial use of architected materials, it is crucial to predict the critical loads at which their mechanical response transitions from linear to nonlinear. The sources of nonlinearity can be multiple, including material nonlinearity and/or multiscale buckling. The set of critical loadings defines a surface in stress or strain space that delineates the region within which the behavior remains elastic, also referred to as the *linearity domain*. This article presents a numerical investigation of the connections between the symmetries of a periodic architected material and the corresponding symmetries of its linearity domain. This investigation yields novel insights: (i) the rotational symmetry order of the linearity domain is directly related to that of the underlying architected material; (ii) the material's chirality manifests itself in the geometry of its linearity domain, which in this case appears tilted; and (iii) the angle of this tilt is correlated with the angle of the parent mesostructure.

Keywords. Symmetry, architected materials, buckling, limit surface.

Funding. These results have been supported by ANR MOMAP ANR-19-CE10-0005 and ANR Max-OASIS ANR-19-CE08-0005.

Note. Article submitted by invitation.

Manuscript received 19 November 2025, revised 16 April 2026, accepted 19 April 2026, online since 4 June 2026.

1. Introduction

Modern engineering challenges have driven the development and adoption of materials organized across multiple scales, enabling greater flexibility in tailoring emergent macroscopic properties — so-called architected materials [1]. These materials exhibit unconventional macroscopic behaviors that arise directly from their geometrical configuration at the mesoscopic scale. This intermediate scale bridges the microscopic level — where the constituent materials are typically

* Corresponding author

regarded as continuous — and the macroscopic scale of the overall structure built from these architected units [2–4]. Empirical studies have shown that architected materials can exhibit remarkable properties, including negative Poisson's ratios [5–7], elastic band gaps [8–10], and enhanced damage tolerance [1,11].

Understanding the link between these unconventional behaviors and the underlying mesoscopic geometry is therefore essential for the optimal design of such materials. These properties predominantly arise within the linear elastic regime; once this regime is exceeded, they degrade and may ultimately lead to material failure. For practical industrial applications, it is therefore crucial to determine the stress or strain range over which the response remains linear, ensuring the preservation of the desired unconventional behavior.

In architected materials, two primary mechanisms can lead to the loss of elastic behavior:

- *buckling-type instability* of the slender elements constituting the internal architecture;
- *nonlinearity of the material behavior*, that is, in practice, the onset of plasticity (in ductile materials), fracture (in brittle materials), or elastic nonlinearity (in hyperelastic materials) [12].

Depending on the case considered, leaving the elastic domain can either lead to the failure of the architected material or produce interesting reconfiguration effects that make it possible to adjust the material's internal geometry to the desired function [7,10,13]. In all cases — whether the objective is to harness or to avoid this behavior — it is essential to identify the boundary separating the linear and nonlinear regimes. In the case of architected materials, the domain of linearity is defined by the interplay between buckling and the limit of mesoscopic linear elasticity.

In [14], the authors observed that, when expressed in a basis associated with the deviatoric and hydrostatic decomposition, the linearity domain of an architected material reflects the symmetries of its underlying mesostructure. Building on this observation, the present work examines the influence of lattice symmetry on the shape of the linearity domain. Following the methodology introduced in [14], we analyze the linearity domains of several two-dimensional lattice materials with different symmetry properties.

The paper is organized as follows: Section 2 provides a concise overview of the definition of the linearity domain and the underlying assumptions used in its computation. Following this, the architected materials under consideration are introduced, along with the tools from symmetry groups theory necessary to describe their symmetry characteristics. Section 3 details the computed domains of linear elasticity and undertakes a comprehensive analysis of their symmetry properties. Section 4 synthesizes the findings and provides insights into prospective extensions, generalizations, and modeling strategies pertinent to the observed phenomena.

2. Linearity domain and studied materials

Throughout the remainder of this paper, we shall work in $\mathbb{R}^2$, and the spaces of strains and stresses will be taken as the space $S^2(\mathbb{R}^2)$ of symmetric second-order tensors, which is isomorphic to $\mathbb{R}^3$.

2.1. *Linearity domain*

This section recalls the definition of the linearity domain [14], summarizes the underlying assumptions used for its computation, and discusses their implications. The linearity domain is a domain of the stress or strain space bounded by a surface known as the limit, or threshold surface. In the present contribution, definitions will be given with respect to strain based formulation, but can be directly adapted to the other situation. In the infinitesimal setting the strain state is given

by $\underline{\underline{\varepsilon}}$, a second-order symmetric tensor known as the infinitesimal strain tensor. This tensor is a point in the vector space $S^2(\mathbb{R}^2)$ which is isomorphic to $\mathbb{R}^3$, meaning that it can be represented as a vector of $\mathbb{R}^3$. The intensity of the strain is evaluated through a function F defined as follows:

$$\begin{aligned} F\colon S^2(\mathbb{R}^2) &\longrightarrow \mathbb{R}^+, \\ \underline{\underline{\varepsilon}} &\longmapsto F(\underline{\underline{\varepsilon}}); \end{aligned} \tag{1}$$

F is an *equivalent strain function.* F may be for instance the max of the principal strains or the hydrostatic strain.

Let us denote by $\varepsilon_{\text{lim}} \in \mathbb{R}_+^*$ the *limit strain* defining the onset of a specific material behavior such as plasticity, damage, buckling or cracking. The limit surface $\mathscr{S}$ in the strain space $S^2(\mathbb{R}^2)$ is the level set $F^{-1}(\varepsilon_{\text{lim}})$:

$$\mathscr{S} := \left\{\underline{\underline{\varepsilon}} \in S^2(\mathbb{R}^2),\ F(\underline{\underline{\varepsilon}}) - \varepsilon_{\text{lim}} = 0\right\}. \tag{2}$$

As long as $F(\underline{\underline{\varepsilon}}) < \varepsilon_{\text{lim}}$, the material remains within its elastic regime. When $F = 0$, the system reaches the boundary of this regime, marking the onset of a transition to other behaviors such as plasticity, damage, or buckling.

Equation (2) constitutes the formal geometric definition of a threshold surface such as the classical Von Mises, Tresca or Morh–Coulomb yield surfaces but stated here in terms of strains instead of stresses.

The practical question, however, concerns the determination of the function F. In general, F need not be explicitly defined as the limit surface $\mathscr{S}$ can be constructed without it but computed numerically, as it is the case for buckling as described below. In the case of a lattice material, this function arises from taking into account two phenomena: (1) buckling of the architecture, and (2) constitutive nonlinearity.

(1) Regarding buckling, it is well established — both experimentally and numerically — that architected materials can exhibit instabilities at multiple scales, particularly in periodic systems [15–20]. Macroscopic buckling corresponds to a global bifurcation of the entire structure, whereas mesoscopic buckling manifests as local geometric changes within the periodic pattern, typically involving one or several unit cells. In addition, localized buckling, confined to a narrow band of cells extending across the specimen, has also been observed. Figure 1 illustrates experimental examples of these three buckling modes. The Bloch-wave analysis [19,21,22] constitutes the most suitable numerical framework for predicting buckling phenomena at any scale in periodic architected materials. Using this approach, several research groups have successfully determined the buckling limit domain for two-dimensional periodic lattices [14,23–25]. This limit domain can be expressed either in terms of stress or strain, with a straightforward conversion between the two as long as the constituent material behaves elastically.

(2) As for the modeling of constitutive nonlinearities, it will here be represented by a Rankine-type criterion applied to the stress within the beams [14]. From a physical standpoint, this framework allows for the modeling of either plastic yielding or fracture of the lattice beams. This approach is not restrictive, and more sophisticated material criteria may also be incorporated.

The linearity domain, defined through the function F, is obtained by combining these two fundamental ingredients as presented now.

Definition 1 (Linearity domain). *The linearity domain of a lattice material, or simply* linearity domain*, is the intersection of the non-buckling domain of the lattice and the linear elasticity domain of its constituent material.*

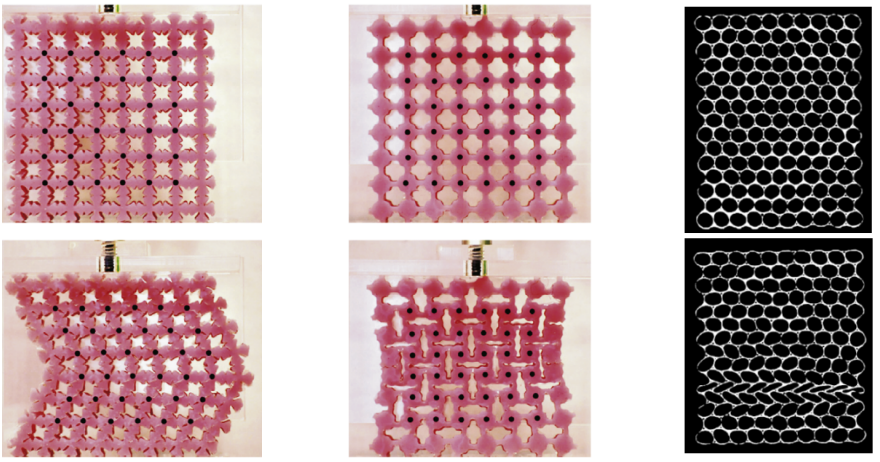

(a) Macroscopic buckling **(b)** Mesoscopic buckling **(c)** Localization

Figure 1. Various types of instabilities observed in architected materials. Figures on the top line correspond to the unloaded material while figures on the bottom line are deformed buckled configurations. Columns (a) and (b) from [17] and (c) from [15].

In the examples discussed in this paper, we focus on lattice materials whose slender cell walls are modeled, in $\mathbb{R}^2$, as Euler–Bernoulli beam elements. The method can, however, be extended to architected materials composed of plate or shell elements, or to more sophisticated beam models, as in [24], for instance. Such extensions would improve the accuracy of the buckling limit prediction but would not significantly alter the overall shape of the linearity domain. The numerical results are obtained using the methodology described in [14] and implemented with the open-source code [26], developed within the MATLAB environment.[1]

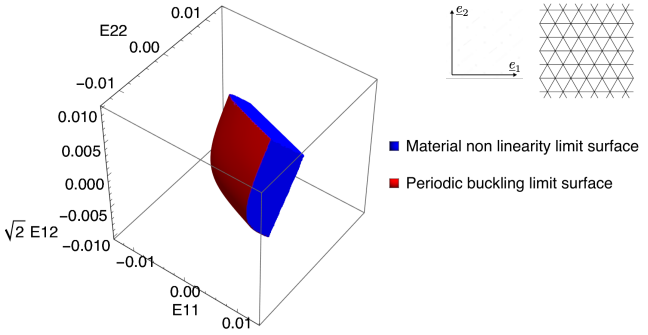

Figure 2. Linearity domain for the equilateral triangle lattice limited by the material nonlinearity limit surface (■) and the periodic buckling limit surface (■) in the spatial tensorial basis of $S^2(\mathbb{R}^2)$. Inset represents the geometry of the studied architected material along with axis of the spatial basis.

An example of a linearity domain combining both the non-buckling and linear-elastic regimes is shown in Figure 2. This result, adapted from [14], concerns a two-dimensional lattice material composed of equilateral triangles made of aluminum. The spatial reference basis, denoted $\mathscr{R}$, and illustrated in the inset of Figure 2, is aligned with the horizontal members of the triangular

[1] For the interested reader the internal parameters considered for the simulation are $n_\eta = 103$, $n_\omega = 500$, $n_\lambda = 1000$, $n_\theta = 30$.

lattice. The macroscopic infinitesimal strain tensor, denoted by $\underline{\underline{E}}$, is defined as the average of the local infinitesimal strain tensors $\underline{\underline{\varepsilon}}$ over the periodic unit cell. The component E_{ij} denotes the projection of $\underline{\underline{E}}$ onto the tensor basis vector $\underline{e}_i \otimes \underline{e}_j$. When expressed in this tensorial basis, the linearity domain does not exhibit any particularly distinctive symmetry features.

Instead of using the tensorial basis constructed from the reference frame, let us consider another basis derived from the deviatoric-spherical decomposition of second-order symmetric tensors. The deviatoric subspace defines a plane whose normal is given by the spherical (or hydrostatic) direction [27]. The deviatoric components of a second-order tensor are obtained from the spatial ones as:

$$E_{d1} = \frac{E_{11} - E_{22}}{\sqrt{2}}, \qquad E_{d2} = \sqrt{2}E_{12}. \tag{3}$$

Figure 3 shows the same linearity domain, now projected onto the deviatoric plane and represented as contour plots for various values along the hydrostatic axis. The contour colors correspond to the material nonlinearity limit surface (■) and the periodic buckling limit surface (■). It can be observed that the contours associated with the material nonlinearity surface form straight lines, as expected from the adoption of a Rankine criterion to model this behavior, whereas those corresponding to the buckling limit surface exhibit a smoother, rounded shape. One can thus clearly observe the tension-compression asymmetry of the linearity domain. Regarding the sections of the domain in the deviatoric plane, they appear to be invariant under a rotation of $\frac{2\pi}{3}$, whereas the geometry of the material itself is invariant under a rotation of $\frac{2\pi}{6}$. This halving of the rotational order is a general property that will be observed in all other cases. Finally, the positions of the symmetry planes in the deviatoric plane seem to be directly related to the symmetry planes of the material.

This article examines how the symmetries of the linearity domain relate to those of the material geometry. To this end, linearity domains are constructed using the procedure introduced

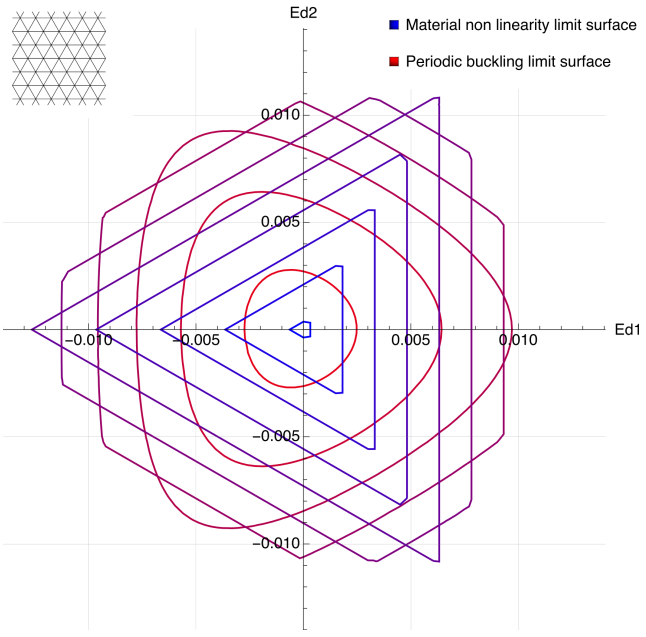

Figure 3. Contours of the linearity domain in the deviatoric plane for different values along the hydrostatic axis. The same color code as in Figure 2 is used.

in [14] for several architected materials exhibiting distinct symmetry characteristics. The following section presents the selected geometries and introduces the notations used to describe their symmetry properties.

2.2. *Choice of studied materials and their symmetries*

This study focuses exclusively on two-dimensional (2D) periodic lattice materials composed of slender, beam-like elements with a constant rectangular cross-section and an isotropic constitutive material. The details of the material and beam properties are provided in Table 1.

Table 1. Constitutive material and beam's properties for the considered architected materials.

Material: aluminum		**Beam's properties**	
Young's modulus	elastic limit	out-of-plane thickness	in-plane thickness
72 GPa	500 MPa	1 mm	1 mm

Under the assumption of uniformity in both material properties and beam geometry, the symmetry of a periodic lattice material coincides with that of its geometric arrangement.

Definition 2 (Symmetries). *Symmetries are defined as the set of isometries of the Euclidean plane that preserve the geometry of the material.*[2]

These isometries can be classified into four types: translations, rotations, reflections, and glide reflections (the latter being a combination of translation and reflection). Among them, rotations and reflections are linear isometries — that is, they fix a point in the affine plane — whereas translations and glide reflections are affine isometries. In $\mathbb{R}^2$, discrete Euclidean groups are commonly referred to as wallpaper groups. According to the crystallographic restriction theorem [28], only 17 distinct wallpaper groups exist.[3]

Linear isometries $\mathbf{g}$ form the orthogonal group, defined as

$$\mathrm{O}(2) \coloneqq \{\mathbf{g} \in \mathrm{GL}(2),\ \mathbf{g}.\mathbf{g}^T = \mathbf{i}\},$$

where GL(2) denotes the group of invertible 2×2 real matrices, and $\mathbf{i}$ is the identity matrix.

Definition 3 (Point group). *The set of linear isometries of a given object $\mathscr{X}$ (tensors, domain...) is a group called the* point group $\mathbf{P}_{\mathscr{X}}$ *of $\mathscr{X}$.*

The space group of a periodic architected material, which is conjugate to one of the 17 wallpaper groups, is obtained by combining the material's point group with its discrete translation group (i.e., its lattice group).

In this work, we investigate the relationship between the symmetry group $\mathbf{G}_{\mathscr{M}}$ of a material and the symmetry group $\mathbf{G}_{\mathscr{D}}$ of its linearity domain. As described in the previous section, the linearity domain $\mathscr{D}$ is a generally compact region defined in the three-dimensional strain (or stress) space. The isometries that leave $\mathscr{D}$ invariant are restricted to linear isometries. The symmetry groups $\mathbf{G}_{\mathscr{M}}$ and $\mathbf{G}_{\mathscr{D}}$ are therefore of different nature. While $\mathbf{G}_{\mathscr{M}}$ is a discrete subgroup of the Euclidean group E(2) meaning that it may contain the four types for isometries defined above, $\mathbf{G}_{\mathscr{D}}$ is a subgroup of the orthogonal group O(3) which contains only linear isometries

[2] Here, the term *Euclidean plane* refers to the *affine Euclidean plane*, i.e. a two-dimensional affine space endowed with a Euclidean metric.

[3] There exist infinitely many discrete isometry groups of the Euclidean plane, but only 17 distinct conjugacy classes, traditionally known as the wallpaper groups.

but of a 3D space. To establish a connection between them, the material $\mathscr{M}$ will be considered only through its point group $\mathbf{P}_{\mathscr{M}}$, hereafter denoted simply as $\mathbf{P}$. The symmetry group of the linearity domain will be regarded only in the deviatoric plane and denoted by $\widetilde{\mathbf{P}}$. More precisely, we will observe the symmetry of the linearity domain in various deviatoric planes defined by their localization along the hydrostatic axis.

Definition 4 (Order of a group). *The order of a group is defined as the cardinality of the set of its elements.*

The entire set of elements of a group can be generated from a smaller subset known as its generators. Depending on their nature, two types of subgroups of O(2) can be distinguished.

Definition 5 (Cyclic group $\mathbb{Z}_n$). *A group generated by a single element* $\mathbf{p}$ *is called a* cyclic group *and is denoted by* $\mathbb{Z}_n$*, where n denotes the order of the group.*

In this study, cyclic groups are used to describe the rotational invariance of a figure with respect to a fixed axis. The corresponding generator, denoted by $\mathbf{r}_n$, represents a rotation through an angle of $\frac{2\pi}{n}$ about the out-of-plane axis. The element $\mathbf{r}_n$ is said to be a rotation of order n, meaning that $\mathbf{r}_n^n = \mathbf{i}$.

Definition 6 (Dihedral group $\mathbb{D}_n$). *A group generated by two elements* $\mathbf{p}$ *and* $\mathbf{q}$ *satisfying*

$$\mathbf{p}^n = \mathbf{i}, \qquad \mathbf{q}^2 = \mathbf{i}, \qquad \mathbf{pq} = \mathbf{qp}^{-1}$$

is called a dihedral group *and is denoted by* $\mathbb{D}_n$*, where n corresponds to the order of the generator* $\mathbf{p}$*. The order of the group is* $2n$*.*

Here, dihedral groups are used to describe the invariance of an object under rotations and reflections with respect to planes containing the axis of rotation. The two generators correspond to $\mathbf{r}_n$, the generating rotation, and $\boldsymbol{\pi}$, one of the generating reflections. When referring to the symmetries of a material, a point group is said to be *chiral* if it does not contain any reflections among its elements; discrete chiral subgroups of O(2) are of type $\mathbb{Z}_n$ [29].

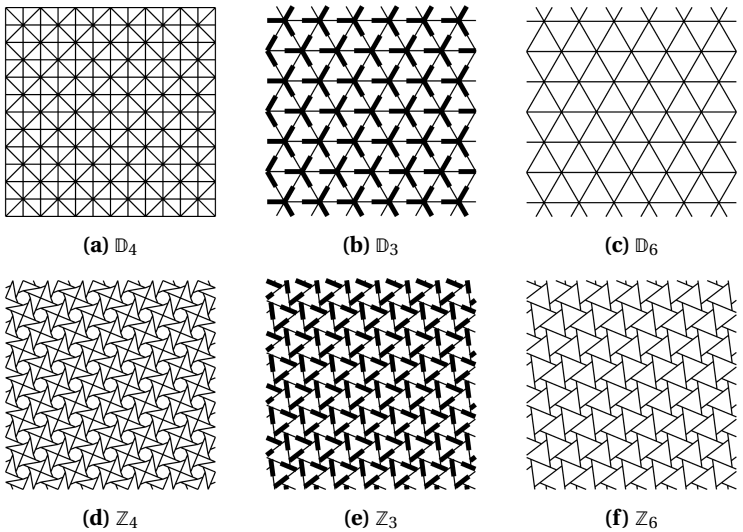

(a) $\mathbb{D}_4$ **(b)** $\mathbb{D}_3$ **(c)** $\mathbb{D}_6$

(d) $\mathbb{Z}_4$ **(e)** $\mathbb{Z}_3$ **(f)** $\mathbb{Z}_6$

Figure 4. The mesogeometry of the six chosen lattice materials studied in this article. The thickness of the lines represent the in-plane thickness of the beams.

In this work, we focus on architected materials exhibiting rotational symmetries of order three or higher and examine how chirality affects the shape of the limit surface. Accordingly, lattice materials with point groups of type $\mathbb{Z}_n$ (chiral) and $\mathbb{D}_n$ (achiral) are considered for $n = 3$, 4, and 6.[4]

The six architected materials considered in this study, denoted according to their point group symmetries, are illustrated in Figure 4. The most symmetric configuration corresponds to the equilateral-triangle lattice, referred to as the $\mathbb{D}_6$ geometry and shown in Figure 4(c). An architected material with point group $\mathbb{D}_4$ was added to verify the relationship between the material's rotational symmetry and its limit surface in the case of even rotational order. For this point group, a reinforced square grid (Figure 4(a)) was chosen instead of a classical square grid in order to ensure adequate shear stiffness. In addition, an architected material with point group $\mathbb{D}_3$ (Figure 4(b)) was included to study the symmetry of its linearity domain when the material's point group exhibits an odd rotational order. This geometry is derived from the hexagonal $\mathbb{D}_6$ lattice, with alternating bars of varying thickness. In Figure 4, the line thickness represents the in-plane beam thickness, set to 1 mm for thin lines and 2 mm for thick ones. Finally, to explore the symmetry of limit surfaces when the parent architected material lacks mirror symmetries, additional chiral geometries with cyclic point groups $\mathbb{Z}_6$, $\mathbb{Z}_4$, and $\mathbb{Z}_3$ were constructed. The $\mathbb{Z}_6$ lattice (Figure 4(f)) corresponds to the chiral geometry originally proposed by Prall and Lakes [30], commonly referred to as the hexachiral structure. Similarly, the $\mathbb{Z}_3$ architected material was derived from the hexachiral geometry by alternating bar thicknesses, following the same approach used for the $\mathbb{D}_3$ case.

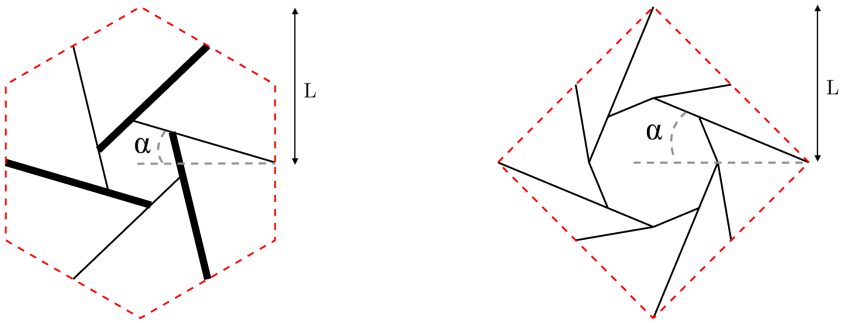

(a) $\mathbb{Z}_3$ **(b)** $\mathbb{Z}_4$

Figure 5. Periodic primitive unit-cells of (a) the $\mathbb{Z}_3$ and (b) the $\mathbb{Z}_4$ architected materials parameterized by the rotation angle α of their central polygon.

By appropriately adjusting the size of the central polygon, these two chiral architected materials can be designed so that the sides of the central polygons remain aligned with the outgoing beams connecting them (see Figure 5). Consequently, they can be parameterized by the rotation angle α of the central polygon, as illustrated in Figure 5 for the example of the $\mathbb{Z}_3$ architecture. The chiral $\mathbb{Z}_4$ architected material (Figure 4(d)) was derived from the reinforced square grid $\mathbb{D}_4$ by applying the same design principle as for the hexachiral geometry. In this configuration perfect alignment of all beams cannot be achieved and was therefore maintained only for the beams

[4] A rotational order of five is incompatible with translational invariance according to the crystallographic restriction theorem.

connecting the corners of the unit cell to the central octagon. Accordingly, the structure was parameterized using the same rotation angle α of the central polygon as described above.[5]

For all the lattice materials considered, the characteristic size of the periodic primitive unit cell is set to $L = 15$ mm. This length corresponds to the beam length for the $\mathbb{D}_6$ and $\mathbb{D}_3$ lattices, to half the diagonal of the primitive unit cell for the $\mathbb{D}_4$ and $\mathbb{Z}_4$ geometries (see Figure 5(b)), and to half the vertical dimension of the hexagonal primitive unit cell for the $\mathbb{Z}_6$ and $\mathbb{Z}_3$ configurations (see Figure 5(a)).

3. Results and discussions

The numerical procedure implemented using the open-source code [26] has been validated against classical benchmark cases, namely the regular square grid as well as the triangular and hexagonal honeycombs. The software successfully reproduces the bifurcated patterns reported in the literature, both numerically and experimentally, and accurately predicts the shape of the non-buckling domain.

The linearity domains computed using this numerical procedure for the six architected materials considered in this study are shown in Figure 6. As in Figure 3, the domains are represented in the deviatoric plane; however, the colored lines now indicate contours corresponding to different values along the hydrostatic axis, ranging from dark blue for the most negative values to bright yellow for the most positive ones. The values along the hydrostatic plane are indicated on the contours.

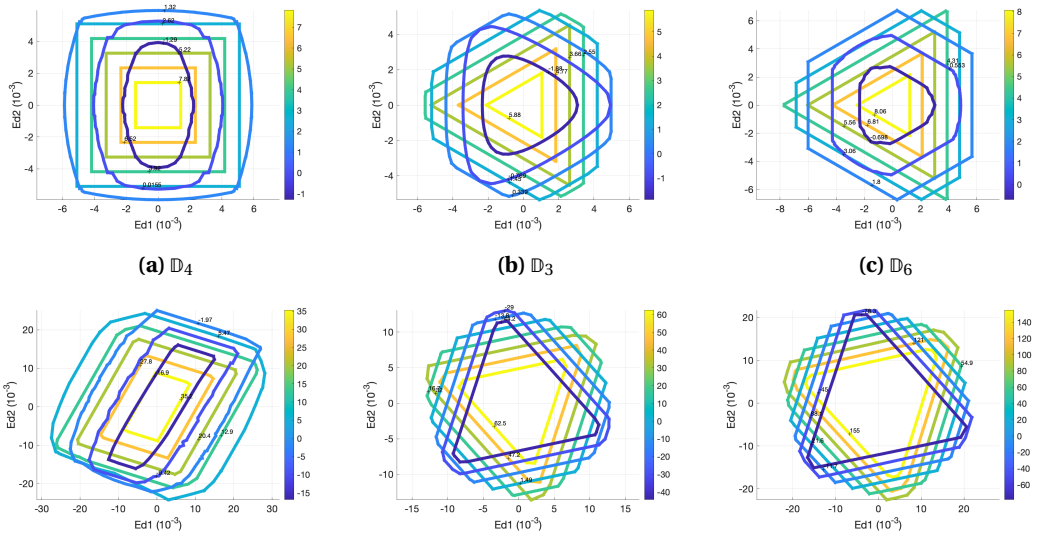

(a) $\mathbb{D}_4$ **(b)** $\mathbb{D}_3$ **(c)** $\mathbb{D}_6$

(d) $\mathbb{Z}_4$ with $\alpha = 18°$ **(e)** $\mathbb{Z}_3$ with $\alpha \approx 16.4°$ **(f)** $\mathbb{Z}_6$ with $\alpha \approx 16.4°$

Figure 6. Contours of the computed linearity domains for the six architected materials considered in this study. The domains are represented in the strain deviatoric plane, with colored lines indicating contours corresponding to different values along the hydrostatic axis (from dark blue for the most negative values to bright yellow for the most positive ones).

[5]The radius of the circumscribed circle of the central octagon was adjusted with the rotation angle α according to $r = \frac{L\sin(\alpha)}{\sin\left(\frac{3\pi}{8}\right)}$.

The main observations drawn from these results are as follows:

(1) for all the materials studied, the contours of the linearity domain present different shapes for different values along the hydrostatic axis;
(2) for all the materials studied, the contours of the linearity domain are predominantly straight lines under positive hydrostatic deformation;
(3) the $\widetilde{\mathbb{D}}_3$ symmetry of the linearity domains associated with both the $\mathbb{D}_3$ and $\mathbb{D}_6$ architected materials is clearly apparent;
(4) the $\mathbb{D}_4$ architected material exhibits a linearity domain with $\widetilde{\mathbb{D}}_2$ symmetry;
(5) the linearity domain of the $\mathbb{Z}_4$ architected material displays $\widetilde{\mathbb{Z}}_2$ symmetry;
(6) the linearity domains of the $\mathbb{Z}_3$ and $\mathbb{Z}_6$ architected materials both exhibit a rotational order of 3;
(7) the chiral or dihedral nature of the linearity domains for the $\mathbb{Z}_3$ and $\mathbb{Z}_6$ materials remains ambiguous;
(8) while the domains of the three dihedral architected materials maintain a fixed orientation in the deviatoric plane, those of the cyclic materials exhibit a noticeable tilt with respect to these axes.

Additionally, it is interesting to note that the $\mathbb{D}_4$ architected material appears to present a linearity domain with $\widetilde{\mathbb{D}}_2$ symmetry for the most positive values along the hydrostatic axis. This phenomenon is a pure coincidence as demonstrated by the same computation using more elongated beams presented in the appendix.

The first observation (1) derives from the multi-criteria nature of the linearity domain. Architected materials tend to buckle under compressive loadings corresponding to negative hydrostatic values while they more easily reach their material nonlinearity limit under positive hydrostatic values. In the case of a material with symmetric tension-compression behavior, one can prove that the resulting linearity domain displays a centrosymmetry property with respect to the center of the strain (or stress) domain [31]. The shape of the contours in the deviatoric plane corresponding to a null hydrostatic state is then peculiar, as it displays the same rotational order as the parent architected material. This feature is not observed in the present case (see Figure 11) because of the dissymmetric nature of the linearity domain which includes a buckling criterion.

As mentioned previously, the second observation (2) directly follows from the use of a Rankine criterion to define the limit of elasticity of the constitutive material.

Recalling that the symmetry group of the architected material is denoted by $\mathbf{G}_{\mathscr{M}}$ and that of the linearity domain by $\widetilde{\mathbf{G}}_{\mathscr{D}}$, the third (3) to sixth (6) observations can be summarized as follows:

$$\mathbb{Z}_n \subset \mathbf{G}_{\mathscr{M}} \quad \Longrightarrow \quad \begin{cases} \widetilde{\mathbb{Z}}_{n/2} \subset \widetilde{\mathbf{G}}_{\mathscr{D}}, & n = 2p, \\ \widetilde{\mathbb{Z}}_n \subset \widetilde{\mathbf{G}}_{\mathscr{D}}, & n = 2p+1, \end{cases} \qquad p \in \mathbb{N}. \tag{4}$$

This implies that when the architected material is invariant under a rotation by an angle θ, its linearity domain is invariant under a rotation by an angle 2θ about the hydrostatic axis. This phenomenon can be explained by the manner in which a rotation in Euclidean space acts on the space of symmetric second-order tensors, such as the stress and strain tensors. Consequently, the relationship expressed in Eq. (4) between the rotational invariance of the mesostructure and that of the linearity domain of an architected material is independent of the constitutive modeling or buckling criteria chosen to describe the mechanical behavior. It is also important to emphasize that this relationship remains valid even when the domain is expressed in terms of stress invariants.

The seventh (7) and eighth (8) observations were further examined by computing the linearity domains for several parameterizations of the $\mathbb{Z}_3$, $\mathbb{Z}_4$, and $\mathbb{Z}_6$ architected materials. Specifically, the parameterizing angle $\alpha = \frac{\pi}{n}$ was varied with $n \in [8, 13]$ for the $\mathbb{Z}_3$ and $\mathbb{Z}_6$ architectures, and

with $n \in [6,10]$ for the $\mathbb{Z}_4$ configuration. The unit cells corresponding to the extreme values of n are shown in Figure 7.

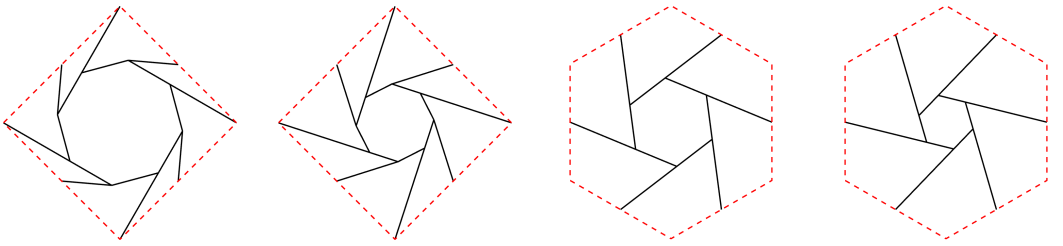

(a) $\mathbb{Z}_4$ with $\alpha = 30°$ **(b)** $\mathbb{Z}_4$ with $\alpha = 18°$ **(c)** $\mathbb{Z}_6$ with $\alpha = 22.5°$ **(d)** $\mathbb{Z}_6$ with $\alpha \approx 13.8°$

Figure 7. Unit cells of architected materials $\mathbb{Z}_4$ and $\mathbb{Z}_6$ for extreme values of parameter α corresponding to (a) $n = 6$, (b) $n = 10$, (c) $n = 8$, (d) $n = 13$.

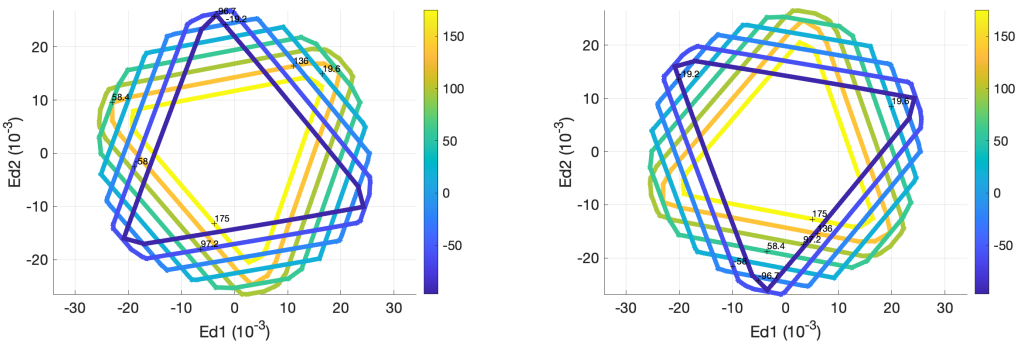

(a) $\mathbb{Z}_6$ **(b)** $\mathbb{Z}_6$ mirrored

Figure 8. Contours of the linearity domains for the $\mathbb{Z}_6$ architected material with $\alpha = 18°$ and the mirror architected material (rotating counterclockwise).

Figure 8(a) shows the linearity domain of the $\mathbb{Z}_6$ architected material for $\alpha = 18°$ (corresponding to $n = 10$). It can be observed that the corners of the dark blue, orange, and forest-green contours are angular, thereby breaking the potential mirror symmetries of these contours. Figure 8(b) presents the linearity domain of the same material but with parent mirrored geometry meaning that the bars surrounding the hexagon now rotate counterclockwise. It can be observed that the linearity domain of the mirrored $\mathbb{Z}_6$ is the same domain as for the original $\mathbb{Z}_6$ material but mirrored with respect to the horizontal axis defined by $E_{d2} = 0$. The complete set of results for this orientation study are presented in the appendix.

The chiral property of the linearity domain is consistently observed across all the chiral $\mathbb{Z}_3$ and $\mathbb{Z}_6$ architectures, confirming the purely cyclic nature of their symmetry. Furthermore, all contours exhibit a common orientation along the hydrostatic axis for the three chiral architected materials, indicating that this orientation remains identical throughout the entire three-dimensional domain.

Figure 9 illustrates the evolution of the slope of the most tilted side of the yellow contour — corresponding to the contour with the highest positive value along the hydrostatic axis — of the linearity domain as the parameterizing angle α increases for the three chiral architected materials.

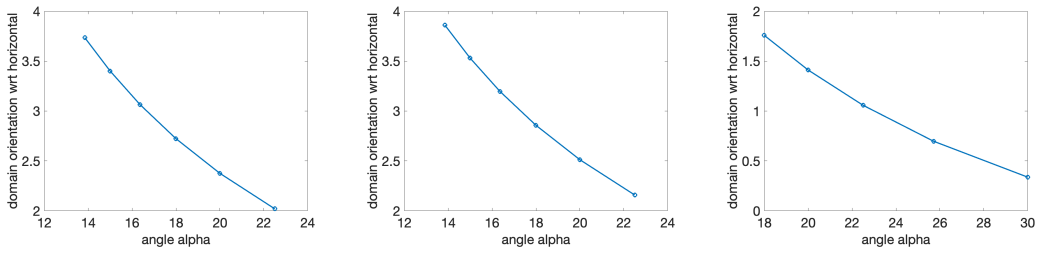

(a) $\mathbb{Z}_3$ **(b)** $\mathbb{Z}_6$ **(c)** $\mathbb{Z}_4$

Figure 9. Variation of orientation of the linearity domain with the angle alpha (in degrees) for the three chiral architected materials.

It can be observed that this slope decreases nonlinearly with the angle α, indicating that the orientation of the linearity domain is correlated with that of the chiral mesostructure. This behavior can be attributed to the sensitivity of both the material nonlinearity and buckling criteria to the relative orientation between the beams and the direction of the applied load transmitted through them. For instance, a load applied along the axis of a beam will trigger buckling at a higher load level than one applied with a tilt. This interpretation is further supported by the observation that the evolution of the linearity domain orientation is similar for the $\mathbb{Z}_3$ and $\mathbb{Z}_6$ architected materials, which share identical beam orientations (see Figure 10).

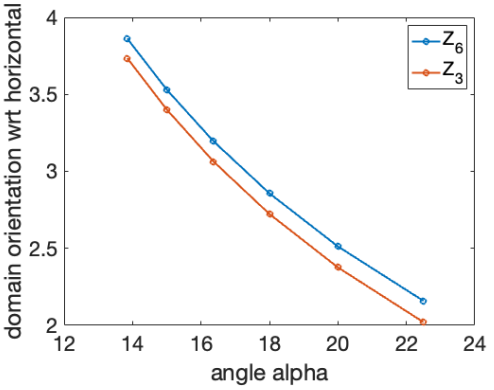

Figure 10. Comparison of evolution of the orientation of domains for the $\mathbb{Z}_3$ and $\mathbb{Z}_6$ architected materials with respect to their parameterizing angle α.

The energy dominance of the architected materials has been verified by finite element analysis. On average, under the considered loadings, the beams composing all the chiral architected materials studied in the main text, and presented in Figure 4, have a larger bending energy compared to their stretching energy. On the contrary, the dihedral architected materials studied presented a predominance of stretching energy in the beams. This type of architected materials are commonly referred to as *stretching-dominated* architected materials [32]. Energy dominance is known to influence some of the emerging macroscopic properties of architected materials [33]. In order to verify that the conclusions drawn in this article are not related to the energy dominance of the architected materials, additional stretching-dominated chiral geometries have been explored. These materials, along with their computed linearity domains, are presented in the appendix. The previously discussed observations remain valid for these cases as well. Moreover, the

chiral nature of the domains appears even more distinctly for these geometries (see, for instance, Figure 16(a)).

4. Conclusion

This study employs numerical simulations to determine the domains of linear elasticity for a variety of two-dimensional architected materials. The objective is to establish a connection between the symmetry of the linearity domain and the symmetry inherent to the mesoscopic configuration of these materials. The results reveal several observations that, to the best of our knowledge, have not yet been reported in the existing scientific literature.

The first observation is that when an architected material is invariant under a rotation by an angle θ, its linearity domain is invariant under a rotation by an angle 2θ about the hydrostatic axis. This phenomenon can be explained using representation theory, by considering how a rotation in Euclidean space acts on the space of symmetric second-order tensors, such as the stress and strain tensors. The second observation is that the dihedral or cyclic nature of the material's point group is directly reflected in the point group symmetry of its linearity domain. Finally, the third observation is that chiral architected materials exhibit linearity domains with a tilted orientation relative to the deviatoric axes, and this tilt is correlated with the orientation of the underlying mesostructure.

In the framework of continuum modeling for architected materials, these observations provide valuable guidance for representing the linearity domain using high-order tensors, as proposed in [31]. Such tensors must be sufficiently rich to capture high-order anisotropy, account for chirality, and represent the asymmetry between tension and compression. A formal identification of the relationship between the observed tilt of the linearity domain and the orientation of the mesostructure is now required. This phenomenon appears to emerge from the mesostructural arrangement at the macroscopic scale and cannot be directly inferred from symmetry group theory, since cyclic groups do not exhibit preferential orientations.

These results would greatly benefit from experimental validation, for instance by confirming the shape of the linearity domain for a given architected material. Likewise, it would be of interest to determine whether the chiral nature of the linearity domain in chiral architected materials arises from the material nonlinearity criterion or from the buckling criterion. These two aspects are currently under investigation by the authors.

Declaration of interests

The authors do not work for, advise, own shares in, or receive funds from any organization that could benefit from this article, and have declared no affiliations other than their research organizations.

Underlying data

The underlying data for this article is available at https://doi.org/10.5281/zenodo.10171789 (see [26]).

Appendix A. Supplementary results

This section presents supplementary results that were excluded from the primary manuscript to facilitate synthesis.

A.1. *Contours of linearity domain for null hydrostatic stress*

The contours of the linearity domains for the deviatoric plane corresponding to a null hydrostatic stress are presented in Figure 11. Note that the contour for the chiral $\mathbb{Z}_3$ architected material is not a regular hexagon as it displays both sharp and rounded vertices, making it $\widetilde{\mathbb{D}}_3$-symmetric.

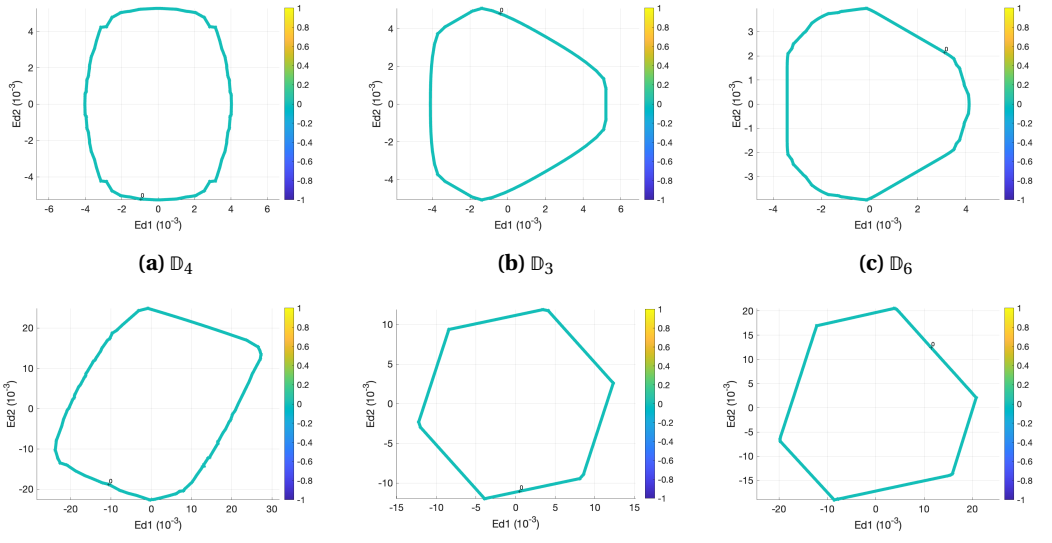

(a) $\mathbb{D}_4$ **(b)** $\mathbb{D}_3$ **(c)** $\mathbb{D}_6$

(d) $\mathbb{Z}_4$, $n = 10$ **(e)** $\mathbb{Z}_3$, $n = 11$ **(f)** $\mathbb{Z}_6$, $n = 11$

Figure 11. Contours of the computed linearity domains for a null hydrostatic stress for all architected materials.

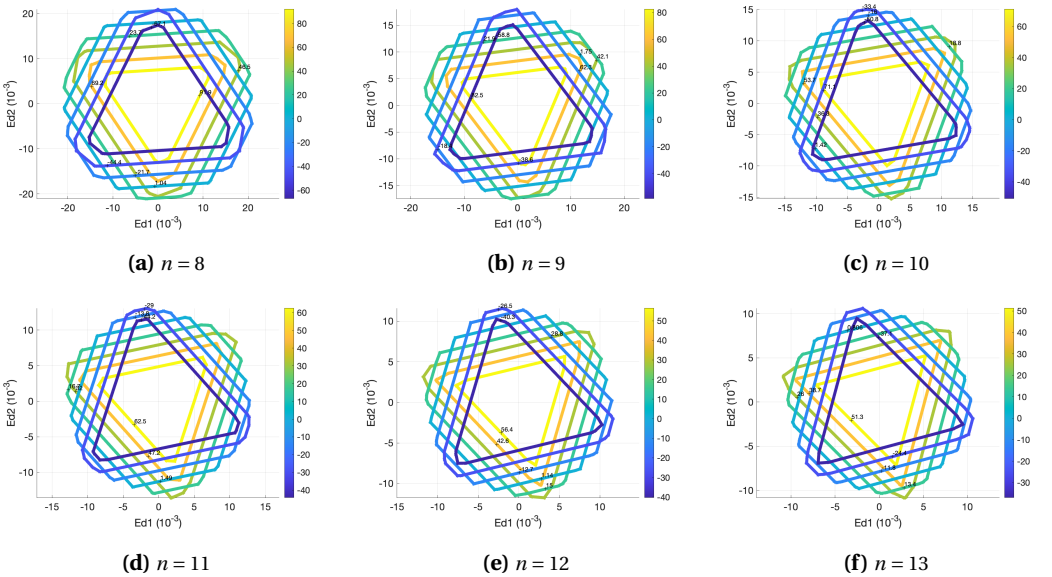

(a) $n = 8$ **(b)** $n = 9$ **(c)** $n = 10$

(d) $n = 11$ **(e)** $n = 12$ **(f)** $n = 13$

Figure 12. Contours of the computed linearity domains for the chiral $\mathbb{Z}_3$ architected materials parameterized by their angle $\alpha = \frac{\pi}{n}$.

A.2. *Orientation study*

The linearity domains computed for the various parameterizations of the $\mathbb{Z}_3$, $\mathbb{Z}_4$, and $\mathbb{Z}_6$ architected materials are presented in Figures 12, 13, and 14, respectively.

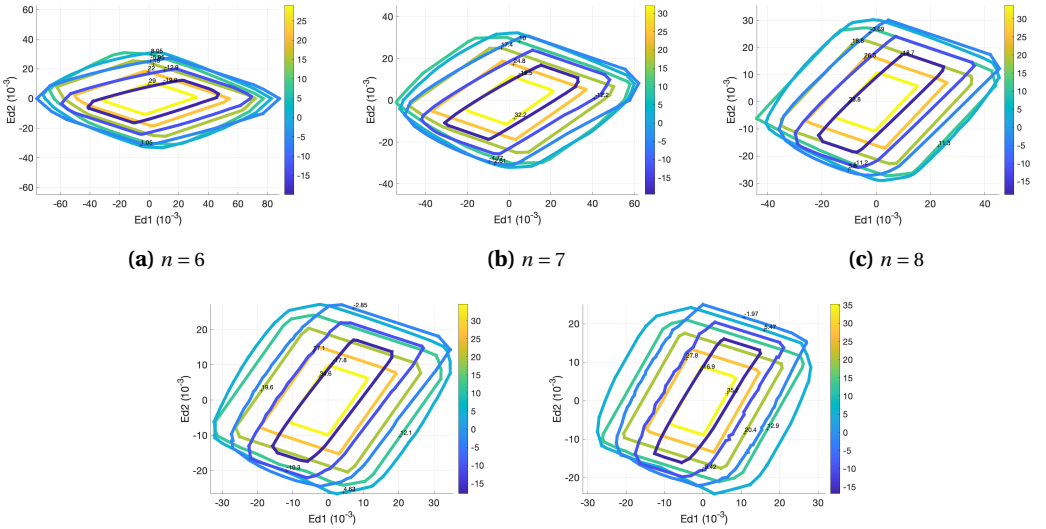

(a) $n = 6$ **(b)** $n = 7$ **(c)** $n = 8$

(d) $n = 9$ **(e)** $n = 10$

Figure 13. Contours of the computed linearity domains for the chiral $\mathbb{Z}_4$ architected materials parameterized by their angle $\alpha = \frac{\pi}{n}$.

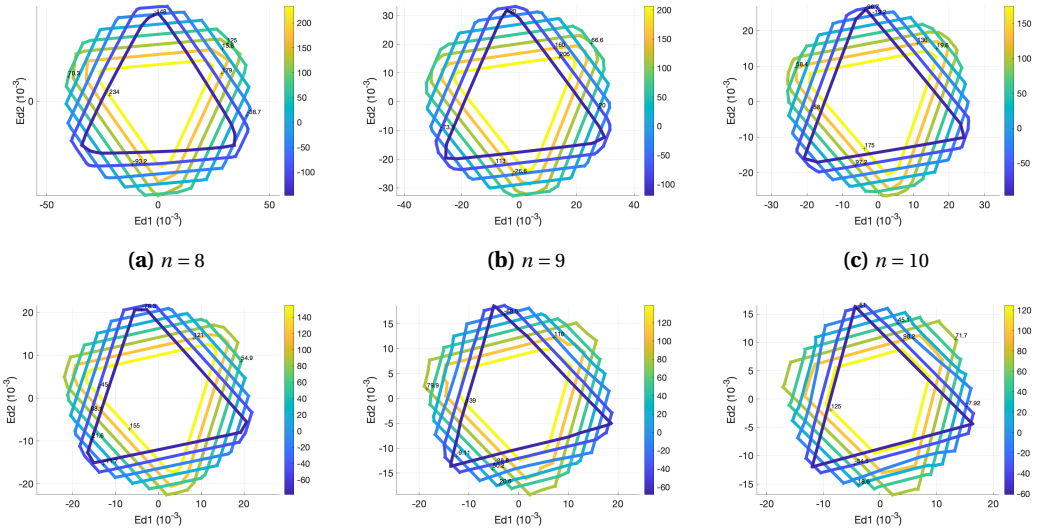

(a) $n = 8$ **(b)** $n = 9$ **(c)** $n = 10$

(d) $n = 11$ **(e)** $n = 12$ **(f)** $n = 13$

Figure 14. Contours of the computed linearity domains for the chiral $\mathbb{Z}_6$ architected materials parameterized by their angle $\alpha = \frac{\pi}{n}$.

A.3. *Stretching-dominated chiral architected materials*

Noting that the selected dihedral architected materials are stretching-dominated [32] — meaning that their beams primarily deform in tension or compression — whereas the designed chiral materials are not (and may, for certain loadings, deform predominantly in bending), additional $\mathbb{Z}_3$ and $\mathbb{Z}_6$ stretching-dominated chiral architected materials were included in the study. Their geometries are presented in Figure 15 and the computed linearity domains are presented in Figure 16.

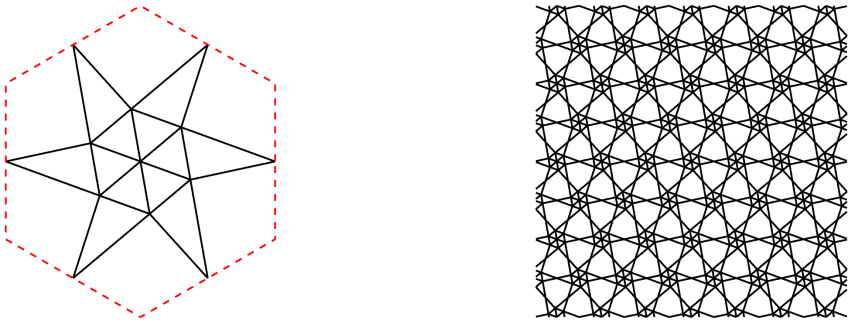

(a) Periodic unit-cell **(b)** Mesogeometry

Figure 15. (a) Periodic unit-cell and (b) mesogeometry of the stretching dominated chiral $\mathbb{Z}_6$ architected material.

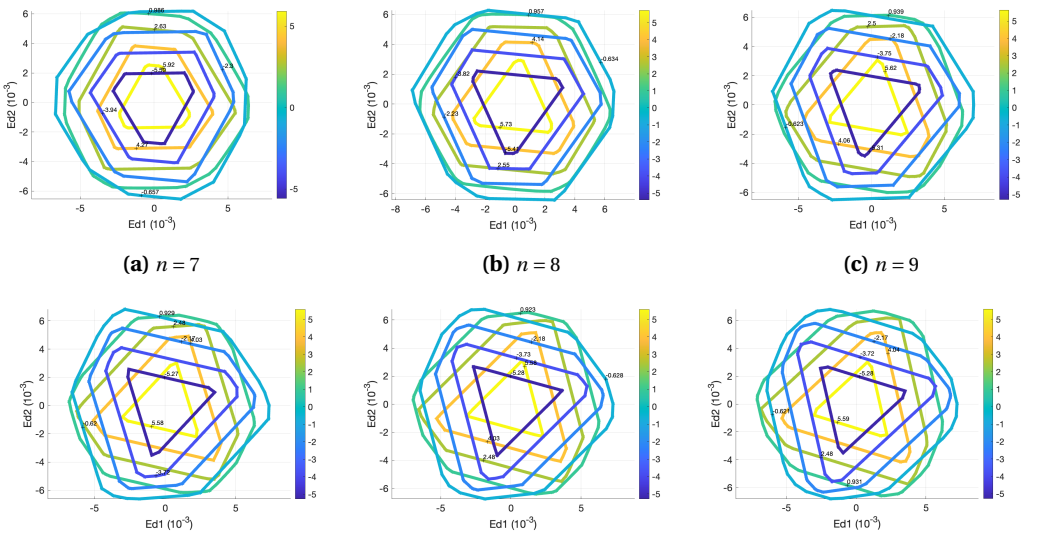

(a) $n = 7$ **(b)** $n = 8$ **(c)** $n = 9$

(d) $n = 10$ **(e)** $n = 11$ **(f)** $n = 12$

Figure 16. Contours of the computed linearity domains for the stretching dominated chiral $\mathbb{Z}_6$ architected material with various orientations referenced by the rotation order n of angle $\alpha = \frac{\pi}{n}$.

References

[1] M. S. Pham, C. Liu, I. Todd and J. Lertthanasarn, "Damage-Tolerant Architected Materials Inspired by Crystal Microstructure", *Nature* **565** (2019), no. 7739, pp. 305–311.

[2] Y. Brechet and J. D. Embury, "Architectured materials: Expanding materials space", *Scr. Mater.* **68** (2013), no. 1, pp. 1–3.

[3] F. Barthelat, "Architectured materials in engineering and biology: Fabrication, structure, mechanics and performance", *Int. Mater. Rev.* **60** (2015), no. 8, pp. 413–430.

[4] M. Poncelet, A. Somera, C. Morel, C. Jailin and N. Auffray, "An experimental evidence of the failure of Cauchy elasticity for the overall modeling of a non-centro-symmetric lattice under static loading", *Int. J. Solids Struct.* **147** (2018), pp. 223–237.

[5] J. Dirrenberger, S. Forest and D. Jeulin, "Effective elastic properties of auxetic microstructures: Anisotropy and structural applications", *Int. J. Mech. Mater. Des.* **9** (2013), no. 1, pp. 21–33.

[6] X. Li, W. Peng, W. Wu, J. Xiong and Y. Lu, "Auxetic mechanical metamaterials: from soft to stiff", *Int. J. Extreme Manuf.* **5** (2023), no. 4, article no. 042003 (26 pages).

[7] A. Ghaedizadeh, J. Shen, X. Ren and Y. M. Xie, "Tuning the performance of metallic auxetic metamaterials by using buckling and plasticity", *Materials* **9** (2016), no. 1, article no. 54 (17 pages).

[8] K. Michielsen and S. Kole, "Photonic band gaps in materials with triply periodic surfaces and related tubular structures", *Phys. Rev. B* **68** (2003), no. 11, article no. 115107 (13 pages).

[9] Y. Chen, H. Yao and L. Wang, "Acoustic band gaps of three-dimensional periodic polymer cellular solids with cubic symmetry", *J. Appl. Phys.* **114** (2013), no. 4, article no. 043521.

[10] P. Wang, J. Shim and K. Bertoldi, "Effects of geometric and material nonlinearities on tunable band gaps and low-frequency directionality of phononic crystals", *Phys. Rev. B* **88** (2013), no. 1, article no. 014304 (6 pages).

[11] L. C. Montemayor, W. H. Wong, Y. W. Zhang and J. R. Greer, "Insensitivity to Flaws Leads to Damage Tolerance in Brittle Architected Meta-Materials", *Sci. Rep.* **6** (2016), article no. 20570 (9 pages).

[12] L. J. Gibson and M. F. Ashby, *Cellular Solids*, Cambridge Solid State Science Series, Cambridge University Press, 1997.

[13] D. M. Kochmann and K. Bertoldi, "Exploiting Microstructural Instabilities in Solids and Structures: From Metamaterials to Structural Transitions", *Appl. Mech. Rev.* **69** (2017), no. 5, article no. 050801 (24 pages).

[14] V. Jeanneau, C. Combescure and M. L. M. François, "Homogenized Elasticity and Domain of Linear Elasticity of 2D Architectured Materials", *Int. J. Solids Struct.* **269** (2023), article no. 112185 (11 pages).

[15] S. D. Papka and S. Kyriakides, "Biaxial crushing of honeycombs — Part 1: Experiments", *Int. J. Solids Struct.* **36** (1999), no. 29, pp. 4367–4396.

[16] R. S. Elliott, "Multiscale Bifurcation and Stability of Multilattices", *J. Computer-Aided Mater. Des.* **14** (2007), pp. 143–157.

[17] J. T. B. Overvelde and K. Bertoldi, "Relating pore shape to the non-linear response of periodic elastomeric structures", *J. Mech. Phys. Solids* **64** (2014), no. 1, pp. 351–366.

[18] Y. He, Y. Zhou, Z. Liu and K. M. Liew, "Buckling and pattern transformation of modified periodic lattice structures", *Extreme Mech. Lett.* **22** (2018), pp. 112–121.

[19] R. Azulay, C. Combescure and J. Dirrenberger, "Instability-Induced Pattern Generation in Architectured Materials — A Review of Methods", *Int. J. Solids Struct.* **274** (2023), article no. 112240 (17 pages).

[20] C. Combescure, "Selecting Generalized Continuum Theories for Nonlinear Periodic Solids Based on the Instabilities of the Underlying Microstructure", *J. Elasticity* **154** (2023), no. 1–4, pp. 421–441.

[21] G. Geymonat, S. Müller and N. Triantafyllidis, "Homogenization of Nonlinearly Elastic Materials, Microscopic Bifurcation and Macroscopic Loss of Rank-One Convexity", *Arch. Ration. Mech. Anal.* **122** (1993), no. 3, pp. 231–290.

[22] K. Bertoldi, M. C. Boyce, S. Deschanel, S. M. Prange and T. Mullin, "Mechanics of Deformation-Triggered Pattern Transformations and Superelastic Behavior in Periodic Elastomeric Structures", *J. Mech. Phys. Solids* **56** (2008), no. 8, pp. 2642–2668.

[23] J. C. Michel, O. Lopez-Pamies, P. Ponte Castañeda and N. Triantafyllidis, "Microscopic and macroscopic instabilities in finitely strained porous elastomers", *J. Mech. Phys. Solids* **55** (2007), no. 5, pp. 900–938.

[24] G. Bordiga, L. Cabras, A. Piccolroaz and D. Bigoni, "Dynamics of Prestressed Elastic Lattices: Homogenization, Instabilities, and Strain Localization", *J. Mech. Phys. Solids* **146** (2021), article no. 104198.

[25] C. Combescure, R. S. Elliott and N. Triantafyllidis, "Deformation patterns and their stability in finitely strained circular cell honeycombs", *J. Mech. Phys. Solids* **142** (2020), article no. 103976.

[26] C. Combescure, M. François, V. Jeanneau and R. Picard, *Elasticity Domain Computation for 2D Architected Materials*, Zenodo, software, v1, 2023. Online at https://zenodo.org/records/10171789.

[27] N. Auffray and P. Ropars, "Invariant-based reconstruction of bidimensional elasticity tensors", *Int. J. Solids Struct.* **87** (2016), pp. 183–193.

[28] R. McWeeny, *Symmetry an introduction to group theory and its applications*, Pergamon Press, 1963.
[29] N. Auffray, J. Dirrenberger and G. Rosi, "A complete description of bi-dimensional anisotropic strain-gradient elasticity", *Int. J. Solids Struct.* **69** (2015), pp. 195–206.
[30] D. Prall and R. S. Lakes, "Properties of a chiral honeycomb with a Poisson's ratio of −1", *Int. J. Mech. Sci.* **39** (1997), no. 3, pp. 305–314.
[31] N. Kesmia, *Optimisation topologique par invariants des structures Lattices anisotropes*, Ph. D. Thesis, Université Gustave Eiffel (France), 2023.
[32] V. S. Deshpande, M. F. Ashby and N. A. Fleck, "Foam topology: Bending versus stretching dominated architectures", *Acta Mater.* **49** (2001), no. 6, pp. 1035–1040.
[33] A. Somera, M. Poncelet, N. Auffray and J. Réthoré, "Quasi-periodic lattices: Pattern matters too", *Scr. Mater.* **209** (2022), article no. 114378.